Engineering Structures 101 (2015) 246–263

Contents lists available at ScienceDirect

# Engineering Structures

journal homepage: www.elsevier.com/locate/engstruct



# Experimental evaluation of the seismic performance of reinforced concrete structural walls with different end configurations

Omar A. El-Azizy [a], Marwan T. Shedid [b], Wael W. El-Dakhakhni [a,*], Robert G. Drysdale [a]

[a] Dept. of Civil Engineering, McMaster Univ., Hamilton, Ontario, Canada
[b] Structural Engineering Department, Ain Shams University, Cairo, Egypt

ARTICLE INFO

*Article history:*
Received 24 December 2014
Revised 25 May 2015
Accepted 22 June 2015

*Keywords:*
Displacement ductility
Reinforced concrete
Seismic response
Structural walls

ABSTRACT

The Canterbury Earthquake Royal Commission report (2013) showed that cantilever reinforced concrete (*RC*) walls failed at a lower ductility capacity than expected due to a plasticity concentration region within a very limited height near the location of the primary cracks at the base of the walls. The New Zealand Standards (*NZS 3101*) (2006) [2] and the Canadian design standards (*CSA A23.3-14*) (2014), adopt the same capacity design approaches for *RC* walls design, with both standards specifying a minimum vertical reinforcement ratios ($\rho_v$%) of 0.25% for *RC* walls. Subsequently, the current study was conducted to study the seismic performance of *RC* walls with different vertical reinforcement ratios and cross sectional configurations. In this paper, six half-scaled *RC* structural walls were constructed and tested under quasi-static displacement controlled cyclic loading. The walls had three different cross sectional configurations; rectangular, flanged and boundary elements and were tested with specific design characteristics selected to evaluate and compare the wall ductility capabilities. In this respect, wall ductility can be defined as the ability of the walls to undergo inelastic deformations with no/low strength degradation, which is essential in Seismic Force Resisting Systems (*SFRS*) as it is not economically feasible to design *SFRS* to behave elastically under seismic loadings. So the ductility quantification of the structural walls used were ductility ratio between the intended displacements with the yield displacement. Based on the test results, the ultimate drift at 20% ultimate strength degradation varied between 0.9% and 1.6% and the ultimate level displacement ductility ($\mu_{\Delta 0.8u}$), ranged approximately between 4.0 and 6.0. Although the flanged walls and the walls with boundary elements were designed to develop almost the same capacity as that of the rectangular walls, the seismic performance of the former wall type was found to be superior to that of their rectangular counterparts with respect to both the ultimate displacement capacity and ductility level. Moreover, using the flanges and the boundary elements walls resulted in approximately 30% reduction of the vertical reinforcement compared to that of the rectangular walls when designed to resist the same lateral loads while carrying identical gravity loads. In addition to gaining insights on the response of walls with boundary elements, the results indicated that structural walls with low vertical reinforcement ratio can experience reduced ductility as indicated in the Canterbury Commission Report.



## 1. Introduction

The Canterbury Earthquake Royal Commission report [1] revealed that some reinforced concrete walls that are designed according to the New Zealand Standards (NZS 3101) (2006) [2] and detailed to comprise the seismic force resisting system of buildings did not achieve their expected ductile capability. The report indicated that the reason was the formation of a primary flexural crack at the expected plastic hinge areas. Such crack might then keep increasing in size as the wall top displacements increase and consequently concentrating the steel plastic strain over a relatively very short height resulting in a premature wall failure at a much lower ductility level compared to what is expected. Such cracking pattern might result in strain concentration of the plastic hinge at a limited zone as well as limiting the generated energy dissipation during seismic event. The report showed that such less-than-expected ductile response was associated with insufficient vertical reinforcement that would have resulted in secondary cracks and higher energy dissipation. Consequently yielding of the

* Corresponding author.
*E-mail addresses:* elazizo@mcmaster.ca (O.A. El-Azizy), Marwan.shedid@eng.asu.edu.eg (M.T. Shedid), eldak@mcmaster.ca (W.W. El-Dakhakhni), drysdale@mcmaster.ca (R.G. Drysdale).

http://dx.doi.org/10.1016/j.engstruct.2015.06.042
0141-0296/

**Nomenclature**

| | |
|---|---|
| *DS* | damage state |
| $f'_c$ | average compressive strengths of concreter cylinders |
| $F_y$ | theoretical yield strength |
| $h_w$ | wall height |
| $l_w$ | wall length |
| $K_{0.8u}$ | stiffness at 20% strength degradation |
| $K_y$ | stiffness at yield |
| $K_u$ | stiffness at the maximum load |
| *MVLEM* | Multiple Vertical Line Element Model |
| $Q_{0.8u}$ | 80% of the experimental maximum capacity |
| $Q_y$ | experimental yield strength |
| $Q_u$ | experimental maximum capacity |
| *RC* | reinforced concrete |
| $R_d$ | ductility related response modification |
| *SFI* | Shear-Flexure Interaction |
| *SFRS* | Seismic Force Resisting System |
| $\Delta$ | target displacement level |
| $\Delta_{0.8u}$ | ultimate level displacement at 20% strength degradation |
| $\Delta_y$ | yield displacement |
| $\Delta_u$ | displacement at the maximum capacity |
| $\mu_{\Delta 0.8u}$ | displacement ductility at 20% strength degradation |
| $\mu_{\Delta}$ | displacement ductility at the maximum capacity ($\Delta_u/\Delta_y$) |
| $\mu^{id}_{\Delta u}$ | idealized displacement ductility at the maximum capacity |
| $\mu^{id}_{\Delta 0.8u}$ | idealized displacement ductility at 20% strength degradation |
| $\rho_h$ | ratio of steel reinforcement in the horizontal direction |
| $\rho_v$ | ratio of steel reinforcement in the vertical direction |

reinforcement was limited to the immediate vicinity of that single primary crack [1]. Subsequently, the report concluded with a recommendation to concentrate the vertical reinforcement ratio $\rho_v$, at the wall end regions to allow for the formation of secondary cracks and to enhance the energy dissipation capabilities by spreading the inelastic straining over a larger length of the outermost wall bars. Such detailing would then increase the wall plastic hinge height and hence, reduce the curvature ductility demands corresponding to different displacement ductility levels.

In addition, observations following the Maule earthquake in Chile (2010), indicated that structural walls showed deficient performance attributed to a combination of high axial loads and high out-of-plane slenderness ratios (small thickness) of the walls [4]. Moreover, Wallace et al. [5], concluded that the unexpected seismic performance in Maule Earthquake was due to the poor web boundary detailing where the strength degraded dramatically because of the buckling of the vertical reinforced after concrete crushing. Similarly, Carpenter et al. [6] concluded that the reason for the low ductile capacities of the structural walls in Maule Earthquake was the poor detailing and confinement. Most of the damaged walls were too thin to be confined which was considered another reason for the poor seismic performance of the structural walls in Maule Earthquake. Within the context of the current study, it might be argued that the small thickness of the walls reported herein was the common parameter between them and those that experienced low seismic performance during the Maule earthquake in Chile (2010).

Thomsen and Wallace [7] tested rectangular and T-shaped structural walls to examine the importance of confinement and transverse reinforcement spacing on the seismic performance of walls. It was concluded that small spacing of the transverse hoops could enhance the ductility of the structural walls. While Thomsen and Wallace [8] used the tested walls to analytically predict the strain profiles where the assumption of the plastic hinge $0.33l_w$ and $0.5l_w$ had a significant impact on the predicted results. Massone and Wallace [9] used the tested walls to assess the wall flexure and shear displacement contributions to the inelastic displacement. The study found that diagonally placed displacement transducer overestimate shear by up to 30% and that there is a strong coupling between inelastic flexural and inelastic shear deformations. Zhang and Zhihao [10] evaluated the seismic behavior of rectangular walls under high axial loading then concluded the negative effect of high axial loading on the walls ductility. Adebar et al. [11] tested *RC* core wall with high axial load and low vertical reinforcement ratio, in order to investigate the effect of cracking on the walls' effective stiffness. Concluded that although there were a large flexure and shear diagonal cracking in the wall, the effective stiffness of the cracked wall was similar to the uncracked wall due to the axial load. Sittipunt et al. [12] tested a series of *RC* walls to investigate the effect of diagonal web reinforcement on the hysteretic curves. They concluded that the diagonal web reinforcement enhance the walls energy dissipation and minimize pinching effect on the hysteretic curves. White [13] developed procedures to estimate the inelastic rotational demand of concrete walls, coupling beam chord rotation and the walls performance with axial yielding. They concluded that for higher period walls the axial demand of coupled walls decreased and walls allowed to yielding in axial tension showed lower coupling beam rotations and energy dissipation capacities.

Beyer et al. [14], tested U-Shaped structural walls in order to evaluate their flexural behavior in different directions. They concluded that the diagonal direction was the most critical direction where the displacement capacity was the smallest. Preti and Giuriani [15], tested a full-scale *RC* wall reinforced with unusual large rebar diameters, uniformly distributed along the wall length. The wall showed high ductility capacity, ensuring a uniform crack pattern and eliminating any localization of crack in the web region. Liao et al. [16], investigated the effect of reinforcing boundary elements walls with Structural steel section in the confined region, where the lateral load capacity increased but failure mode could only change from shear to a mixed flexure-shear mode when the aspect ratio (height/width) was three or more. Oh et al. [17] studied the effect of confinement and end-configurations of Reinforced Concrete structural walls, where they tested three rectangular and a barbell shaped walls. They concluded that the barbell and the well-confined rectangular wall showed similar ductility and energy dissipation.

Orakcal and Wallace [18] proposed a Multiple Vertical Line Element Model (*MVLEM*) to predict the flexural response of *RC* structural walls under cyclic loading. The model was designed to successfully capture *RC* walls cyclic response including the stiffness degradation, strength deterioration and hysteretic shape. Orakcal and Wallace [19] compared the *MVLEM* results with the experimental results and the model was capable of predicting the capacities, average rotations over the region of inelastic deformations, and neutral axis position. However, the *MVLEM* underestimated the compressive strains and was not accurate in predicting the non-linear tensile strain distributions in the flanges of T-shaped walls. Kolozvari et al. [20] proposed a model to accurately capture the nonlinear flexural/shear interaction of the cyclic response of reinforced concrete structural walls. The model successfully captures the hysteretic loops of the overall load–displacement relationship. Kolozvari et al. [21] experimentally calibrated and validated the analytical model proposed with five moderately slender reinforced concrete walls experiencing extensive levels of shear-flexure interaction. Concluded that the Shear Flexure Interaction (*SFI*) *MVLEM* was effective in predicting the contribution of the flexural and shear of the lateral deformation along the height of the *RC* structural walls.

Other researchers [22–24] discussed the seismic codes provisions by quantifying the plastic hinge length, the methodology behind proposed ductility related modification factors and shifting to performance-based design. Mitchell et al. [25] and Adebar et al. [26], carried out studies to compare between the different versions of the Canadian seismic code provisions, corresponding to shear wall design, over the last few decades.

The shake table testing reported by Ghorbanirenani et al. [27] showed that the peak base shear force developed prior to any significant inelastic wall rotations and that walls experienced limited inelastic flexural deformations at their bases. In addition, the maximum inelastic rotation did not occur simultaneously with the maximum roof displacement. The study also reported inelastic flexure response at due to higher modes effects. Subsequently, the study recommended consideration of inelastic flexure response further away from the wall base, due to higher modes effects, in future design provisions. Lu et al. [28] concluded that the current provisions of National Building Code of Canada (*NBCC*) *2010* [29] and *CSA A23.3-14* [3] underestimated the wall base shear force demands by 15–70%. In addition, they indicated that future design provisions should consider amplifying the design bending moments above the plastic hinge region in order to constrain the plastic deformation to the plastic hinge region at the base of the wall.

The objective of the current study is to investigate, how the level and distribution of vertical reinforcement can influence the wall failure mechanism as discussed in the Canterbury earthquake report. This is important as it is usually expected that walls with low vertical reinforcement ratios would posses higher ductility capacities than walls with higher vertical reinforcement ratios; which was not the case during the Canterbury earthquake.

## 2. Experimental program

The experimental program was conducted to quantify the influence of configuration and vertical reinforcement ratio on the ductile capabilities of *RC* structural walls. A fully reversed cyclic displacement-controlled load was applied quasi-static to the top of the walls as shown in Fig. 1 while the wall was being subjected to a constant axial load throughout the test. The testing of each wall was terminated when the maximum capacity degraded to approximately 50%. All the walls were detailed as ductile structural walls according to the *CSA A23.3-14* [3]. The following sections highlight the material properties, design, construction, test setup and instrumentation. This is followed by a discussion of the failure modes, load–displacement relationships, displacement ductility and strength and stiffness degradations.

### 2.1. Test matrix and wall design criteria

*Phase I* walls (*W1*, *W2*, *W3*) were designed to have approximately the same strength, while having same overall dimensions and being subjected to the same axial load, in order to facilitate a direct comparison between their displacements and ductility capabilities. The same comparison can be conducted to the *Phase II* walls (*W4*, *W5*, *W6*) as they were also designed to have approximately the same strength, yet different reinforcement ratios from those tested in *Phase I*.

The six half-scaled *RC* walls (two rectangular, two flanged, and two with boundary elements) were constructed with the same overall dimensions but different cross sections as shown in Fig. 2. *Phase I* walls vertical reinforcement ratios ($\rho_v$) of the rectangular Wall *W1*, the Flanged Wall *W2*, and the Wall with boundary elements *W3* were 1.17%, 0.66%, and 0.69%, respectively. For the other three (*Phase II*) walls, as listed in Table 1, the vertical reinforcement ratios were 2.80%, 1.58% and 1.63% for the rectangular Wall *W4*, the flanged Wall *W5*, the wall with boundary elements *W6*, respectively. All walls characteristics are listed in Table 1. All the walls were reinforced with two layers of vertical reinforcements, which limited out-of-plane displacement and increased the stability when the walls were under inelastic strains [30].

All walls were horizontally reinforced to resist the lateral shear load according to the *CSA A23.3-14* [3] provisions. As such, *Phase I* rectangular wall horizontal reinforcement ratio ($\rho_h$) was 0.63%, whereas the corresponding horizontal reinforcement ratio for *Phase I* flanged and boundary elements walls was 0.55%. With the expected higher capacities of *Phase II* walls (due to the increased flexural reinforcement ratios), $\rho_h$ was 1.28% for the rectangular wall and 1.05% for the flanged and boundary elements walls. Confinement ties were detailed and spaced according to the *CSA A23.3-14* standards [3] for buckling prevention. Where the confinement reinforcement spacing (at half-scale) was 55mm for the boundary elements Wall *W6* and was 45mm for the remaining walls. In the heavily reinforced region, each vertical reinforcement was laterally supported by the corner of tie or an inclined angle of not more than 135° as specified by the *CSA A23.3-14* [3] as shown in Fig. 2.

It is worth noting that the addition of flanges and boundary elements to the walls and the concentration of part of the reinforcement at the wall ends resulted in approximately 30% reduction of the vertical reinforcement as opposed to their rectangular counterparts.

### 2.2. Material characteristics

The walls concrete was poured in two stages. The maximum aggregate size was 10 mm for the six half-scale walls. Twelve concrete cylinders with a diameter of 150 mm and a height of 300 mm were prepared and tested under compression from each pour [31]. The cylinders were tested at the ages of 7, 14, 28 days and just prior to wall test. The average concrete compressive strengths for all the walls are listed in Table 2(a). The use of the same concrete for all the three walls was intended to facilitate the comparison between rectangular, flanged and boundary elements walls.

The half-scaled versions of *M10*, *M15*, *M20* (100 $mm^2$, 200 $mm^2$ and 300 $mm^2$, respectively) bars used to reinforce the test walls were, respectively, *D4*, *D7* and *D11* bars having cross sectional areas of 26 $mm^2$, 45 $mm^2$ and 71 $mm^2$, respectively as shown in Table 2(b). The *D4* bars were used as the horizontal reinforcements for all the walls and were used as the distributed vertical reinforcements for Walls *W2* and *W3*. The *D7* bars were used as vertical reinforcement in the outer parts of *W2* and *W3*, throughout the entire cross section of *W1*, and on the inner parts of *W5* and *W6*. Finally, the *D11* bars were used as the vertical reinforcements of Wall *W4* throughout the section and on the outer parts of the heavily reinforced areas of Walls *W5* and *W6* as shown in Fig. 2(e) and (f).

Three 600 mm test coupons of each bar size were tested under tension following ASTM A615-09 [32]. The average yield strength of the *D4* and *D7* bars were 510 MPa (*c.o.v.* = 3.5%) and 480 MPa (*c.o.v.* = 2.8%), respectively, with elongation of 8.0%, and 10.7%, respectively. The D11 bars had an average yield

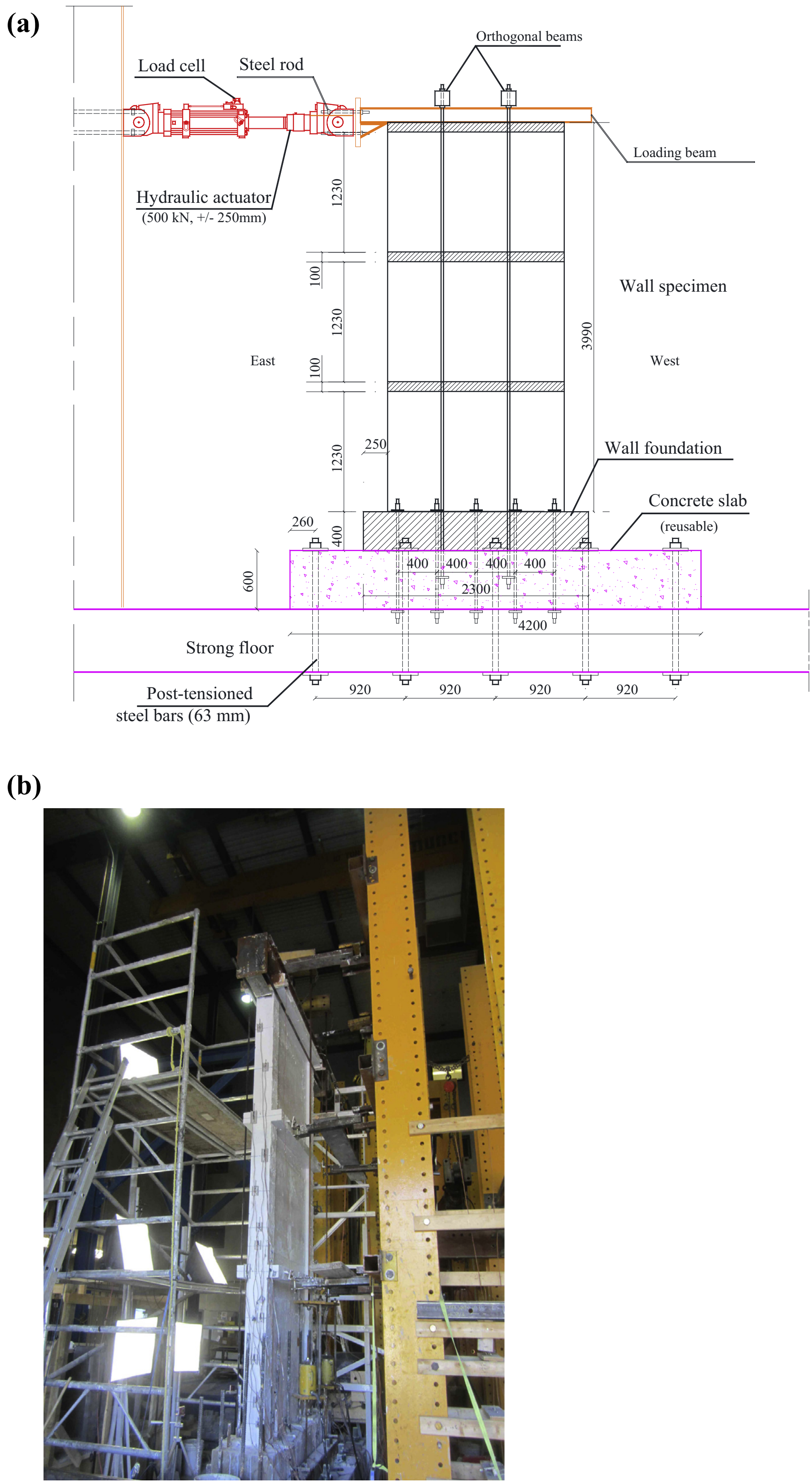


**Fig. 1.** (a) Test setup: face view; (b) test setup: side view.

strength of 420 MPa (*c.o.v.* = 6.9%) and 9.4% elongation. The average ultimate strength of *D*4, *D*7 and *D*11 bars were 556 MPa (*c.o.v.* = 3.4%), 526 MPa (*c.o.v.* = 2.1%) and 511 MPa (*c.o.v.* = 4.2%), respectively.

### *2.3. Construction, test setup and instrumentation*

All the walls consisted of three-story with the same overall height and width (3990 mm $\times$ 1802 mm). The height of each story

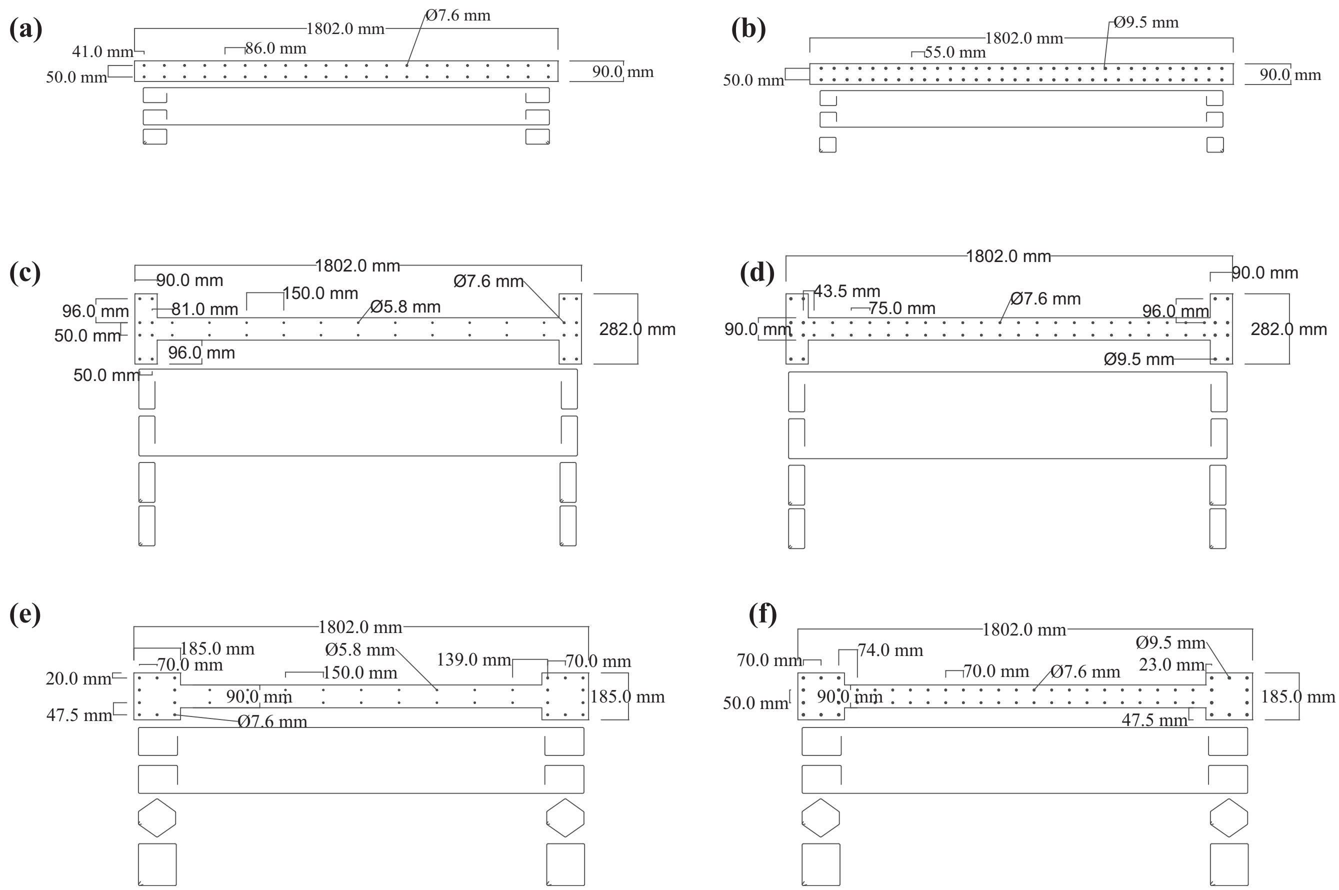


**Fig. 2.** Specimens configurations; rectangular walls (a) *W1* & (b) *W4*; flanged walls (c) *W2* & (d) *W5*; boundary elements walls (e) *W3* & (f) *W6*.

**Table 1**
Test matrix.

| Specimen | Configuration | Wall dimensions | Vertical reinforcements | | Horizontal reinforcements | | Axial stress (MPa) | Axial (% $f'_c$) |
|---|---|---|---|---|---|---|---|---|
| | | | Number of bars and bar sizes | $\rho_v$ (%) | D4 at spacing (mm) | $\rho_h$ (%) | | |
| *W1* | Rectangular | 1802 mm × 3990 mm length × height | 42 D7 | 1.17 | 2 at 90 | 0.64 | 1.09 | 3.85 |
| *W2* | Flanged | | 16 D7 & 22 D4 | 0.66 | 2 at 110 | 0.53 | 0.89 | 3.15 |
| *W3* | Boundary elements | | 20 D7 & 18 D4 | 0.69 | 2 at 110 | 0.53 | 0.89 | 3.15 |
| *W4* | Rectangular | | 64 D11 | 2.80 | 2 at 45 | 1.28 | 1.09 | 2.66 |
| *W5* | Flanged | | 16 D11 & 44 D7 | 1.58 | 2 at 55 | 1.05 | 0.89 | 2.17 |
| *W6* | Boundary elements | | 20 D11 & 40 D7 | 1.63 | 2 at 55 | 1.05 | 0.89 | 2.17 |

was 1230 mm in addition to 100 mm slab thickness extending 150 mm in both out-of-plane sides as shown in Fig. 1. The vertical reinforcement of the wall was extended and bent into the foundation extending 250 mm from each side of the wall. The *RC* foundation had a width of 2300 mm, height of 400 mm and depth of 500 mm. The concentrated reinforcement regions at each end had one rectangular tie for Walls *W1* and *W4* while two rectangular ties were used for Walls *W2* and *W5*. Regarding Walls *W3* and *W6* two ties (rectangular and hexagonal) were used on each end as shown in Fig. 2.

Each wall was placed on the reusable slab in the test setup as shown in Fig. 1(a). A built-up steel U-shaped loading beam was connected and coincided to the hydraulic actuator to uniformly transfer the simulated earthquake loading on the entire length of the wall as opposed to a concentrated load at the wall corner. The lateral cyclic loading of the wall was applied using a displacement-controlled hydraulic actuator with a maximum stroke of ±250 mm and a maximum capacity of ±500 kN. Six out-of-plane steel sections were connected to the wall for lateral stability as shown in Fig. 1(b). The out-of-plane members were designed and installed to prevent out-of-plane movement while allowing lateral movements and rotations in the in-plane directions.

The axial load was incorporated in the test via two force-controlled hydraulic actuators, which were connected to four threaded rods (two from each side of the box section) as shown in Fig. 1. The applied load on each rod was maintained at 40 kN resulting in a total vertical axial load on the wall of 160 kN.

Thirty-eight displacement potentiometers were used to measure and record the sliding, vertical, and lateral displacements at

**Table 2**
Materials (a) concrete strengths and (b) reinforcements.

| Concrete | Compressive strength (MPa) | C.O.V. (%) | Standard |
|---|---|---|---|
| *(a)* | | | |
| Walls *W1* and *W2* | 28.3 | 5.5 | Cylinder Test ASTM C39–10 |
| Wall *W3* | 36.4 | 3.4 | Cylinder Test ASTM C39–10 |
| Phase II Walls | 41.0 | 7.3 | Cylinder Test ASTM C39–10 |

| Reinforcement | Area ($mm^2$) | Yield strength (MPa) | C.O.V. (%) | Elongation (%) | Standard |
|---|---|---|---|---|---|
| *(b)* | | | | | |
| D4 | 26 | 510 | 3.5 | 8.0 | ASTM A615-09 |
| D7 | 45 | 480 | 2.8 | 10.7 | ASTM A615-09 |
| D11 | 71 | 420 | 6.9 | 9.4 | ASTM A615-09 |

various points on the wall. Fourteen electrical strain gauges were attached to the four outermost vertical reinforcement bars. The strain gauges locations for the first two bars were placed 200 mm below the interface between the wall and the foundation, at the interface, at 100 mm above the interface, at a height of 900 mm corresponding to half of the length of the wall ($l_w/2$) and at a height of 1800 mm ($l_w$). The second two bars had one strain gauge 50 mm above the interface and at a location equal to the length of the wall 1800 mm ($l_w$).

The strain gauges located below the interface and in the foundation were used to determine the extent of plasticity in the foundation which could significantly affect wall top displacement as discussed by Priestley et al. [33] and Shedid and El-Dakhakhni [34].

A target wall resistance equal to 20% of the theoretical yield load $F_y$ was considered in the first loading cycle and was followed by target resistance of 40%$F_y$, 60%$F_y$ and 80%$F_y$. The loading was then continued until the experimental yield load $Q_y$ and corresponding top wall displacement $\Delta_y$ were determined. After reaching the yield strength, displacement controlled loading, based on multiples of the experimentally determined yield displacement was followed until the wall resistance degraded to approximately 50% of its maximum values, at which point the test was terminated.

## 3. Test results

The walls lateral load capacities, load–displacement relationships, crack patterns, failure modes, load–displacement envelopes and stiffness degradation are presented and discussed in the following sections. In addition, the displacement ductility values for each wall were computed and compared.

### 3.1. Lateral load capacities

The theoretical and experimental yield strength, $Q_y$ and ultimate flexural strength $Q_u$, for all walls were listed in Table 3. Using mechanics, the strength predictions, ignoring material or strength reduction factors, were determined according to the *CSA A23.3-14* [3] by limiting the extreme fiber compressive strain for concrete to 0.0035. The predicted yield loads for *Phase I* walls were slightly conservative while *Phase II* predicted yield loads were more in agreement with the experimental results. On the other hand, predicted ultimate strengths of all the specimens were similar to the experimental results except in Wall *W1* where a construction error occurred at the East Toe as explained earlier. While, the difference in the push direction can be due to strain hardening of the vertical reinforcements *D*7 bars.

### 3.2. Wall load–displacement relationships and failure modes

The load–displacement hysteresis relationships of all the test walls are plotted in Fig. 3. The yield load $Q_y$ and ultimate load $Q_u$ are shown in the push and pull directions on each hysteresis loops graph. A table is inserted in each graph to show the yield load $Q_y$, the maximum load $Q_u$, and load at 20% strength degradation $Q_{0.8u}$, along with their corresponding displacements. The bottom right table in each graph shows the wall key features including: the wall length, $l_w$, height, $h_w$, vertical, $\rho_v$, horizontal, $\rho_h$, reinforcement ratios as well as the axial load, $P$, applied on the wall. The top right quadrant shows the load–displacement relationships in the push direction where the East toe was under tension and the west toes was under compression and vice versa as it is seen for the bottom left quadrant. Prior to yielding, the slope of the hysteresis loops indicated higher stiffness of the wall compared to loading beyond yield where the slopes of the loading portion of the hysteresis loops of each cycle showed gradual stiffness degradation for all walls. The hysteresis loops after yield started widening which would increase energy dissipation capabilities for walls. In general, all walls failed in a flexural manner characterized by crushing of the concrete at the toes followed by buckling of the vertical bars and finally the outermost vertical reinforcements fractured and the wall strength degraded significantly.

#### 3.2.1. Wall W1

The hysteresis loops for Wall *W1* are shown in Fig. 3(a). First yield at the outermost bars was recorded at 152 kN and 123 kN in the push and pull directions, respectively corresponding to displacements of 7.4 mm and 9.2 mm in the push and pull directions, respectively. The average yield displacement taken as $\Delta_y$ = 8.4 mm (0.21% drift) was then selected to determine the target displacement levels as multiple of yield displacement.

The recorded ultimate load $Q_u$ was 230 kN in the push and 172 kN in the pull loading direction corresponding to a top displacement of 22.7 mm (0.57%) and 17.1 mm (0.43%), respectively. The wall reached its ultimate load at 3$\Delta_y$ during the push cycle, while in the pull loading direction the wall reached its ultimate strength during the 2$\Delta_y$ loading cycle. The variability in the strength and displacement could be in part due to an accidental problem during the concrete pouring as minor voids were discovered at the East toe of the wall and were later repaired using high strength low shrinkage repair mortar as they were necessary prior to testing. At 4$\Delta_y$ (0.84% top drift), the concrete crushed during the first loading cycle at both wall toes and during the second loading cycle 3 vertical reinforcement bars fractured in the East end of the wall as listed in Table 4 (where repair mortar was used). At 5$\Delta_y$ loading cycle corresponding to 42.0 mm (1.05% drift), 5 outermost West vertical bars fractured. The wall was then loaded even further to 6$\Delta_y$ (1.26% drift) were both corners were heavily damaged as shown in Fig. 4(a) and the test was terminated.

#### 3.2.2. Wall W2

The experimental yield $Q_y$ load for wall *W2* was 175 kN and 158 kN in the push and pull directions, respectively and corresponded to displacements of 8.9 mm (0.22% drift) and 8.4mm (0.21% drift), respectively. Due to a minor error in identifying the actual yield displacement $\Delta_y$ while testing, the wall was pushed in multiples of 10 mm. At 2.3$\Delta_y$ (0.50% drift) the wall reached its maximum capacity of 187 kN in the push and 183 kN in the pull directions as shown in Fig. 3(c). At 4.6$\Delta_y$ (1.00% drift) displacement level, concrete crushed at the flanges, the vertical bars buckled and the first bar fractured. The ultimate level displacement $\Delta_{0.8u}$ was reached in the push direction at 0.70% top drift while at 0.95% top drift in the pull direction. When the wall was loaded to 5.8$\Delta_y$ (1.25% drift), all the bars in the flanges fractured, in addition to

**Table 3**
Summary of predicted and measured strengths.

| Specimen | Configuration | Yield strength $Q_y$ | | | | | Maximum capacity $Q_u$ | | | | |
|---|---|---|---|---|---|---|---|---|---|---|---|
| | | Predicted (kN) | Measured (kN) | | Difference (%) | | Predicted (kN) | Measured (kN) | | Difference (%) | |
| | | | Push (+ve) | Pull (−ve) | Push (+ve) | Pull (−ve) | | Push (+ve) | Pull (−ve) | Push (+ve) | Pull (−ve) |
| *Phase I* | | | | | | | | | | | |
| *W1* | Rectangular | 136 | 152 | 123 | 11 | 11 | 193 | 230 | 172 | 16 | 12 |
| *W2* | Flanged | 136 | 175 | 158 | 22 | 14 | 177 | 187 | 183 | 5 | 3 |
| *W3* | Boundary elements | 135 | 161 | 160 | 16 | 16 | 178 | 176 | 177 | 1 | 1 |
| *Phase II* | | | | | | | | | | | |
| *W4* | Rectangular | 233 | 222 | 195 | 5 | 19 | 351 | 336 | 355 | 4 | 1 |
| *W5* | Flanged | 218 | 220 | 270 | 1 | 19 | 330 | 322 | 313 | 2 | 5 |
| *W6* | Boundary elements | 213 | 227 | 209 | 6 | 2 | 332 | 334 | 313 | 1 | 6 |

the 8 outermost bars in the East and the 10 outermost bars in the webs in the west side. At this point the wall strength degraded more than 50% of the maximum capacity and the test was terminated.

This wall did not show the expected ductility due to a localized failure at the interface between the wall and the foundation. The interface crack started opening up and the tensile steel strain and plastic deformations were concentrated at the bottom of the wall as evident from the cracking pattern in Fig. 4(b).

### 3.2.3. Wall W3

The experimental yield strength of wall *W3* occurred at a load of 160 kN with a displacement $\Delta_y$ equal to 8.5 mm (0.21% top drift) and 8.1 mm (0.20% top drift) in the push and pull directions, respectively. The maximum recorded strength of the wall was 176 kN and 177 kN in the push and pull directions, respectively and was reached corresponding to $2\Delta_y$ (0.42% drift) displacement level, as shown in Fig. 3(e). At $4\Delta_y$ (0.84% drift) displacement level, the concrete around the boundary elements crushed and the bars buckled as listed in Table 4. In the second cycle of $4\Delta_y$ (0.84% drift) loading two bars fractured in the pull direction. The ultimate level displacements of the wall were 1.00% and 0.90% (top drift) in the push and pull directions, respectively. When the wall was pushed to displacement level of $5\Delta_y$ (1.05% drift) two bars fractured on each direction as shown in Fig. 4(c). The wall was further pushed to $6\Delta_y$ (1.26% drift) and all the bars in the boundary elements fractured in both directions and the strength degraded to less than 50% of the maximum capacity so the test was terminated.

The wall showed an unexpected moderate ductility compared to what was expected. However, due to a lift-up in the interface after concrete crushing in the boundary elements, the outermost reinforcement strained plastically at the interface crack. The unexpected moderate ductility stated earlier as the enhancement in the ductility of boundary elements wall *W3* compared to rectangular wall *W1* was lower than the enhancement of boundary elements wall *W6* when compared to rectangular wall *W4*.

### 3.2.4. Wall W4

The hysteresis loops for wall *W4* are shown in Fig. 3(b). The first crack in the wall occurred at 60% of the theoretical yield strength, $F_y$. The wall experimental yield loads were 222 kN in the push and 195 kN in the pull corresponding to top displacements of 12.6 mm (0.32% top drift) and 9.2 mm (0.23% top drift), respectively. The maximum strength of the wall was recorded at $3\Delta_y$ (0.84% drift) displacement level, and was equal to 336 kN in the push and 355 kN in the pull. At the second cycle of $3\Delta_y$ (0.84% drift) chunks of concrete spalled at both ends as listed in Table 4. As the wall was approaching to $4\Delta_y$ (1.13% drift) displacement level, concrete crushing occurred in the compression side and 2 of the outermost vertical bars fractured in the tension side as shown in Fig. 4(d). The strength of the wall then degraded rapidly to 191 kN and 248 kN in the push and pull cycles, respectively. At the second cycle of $4\Delta_y$ (1.13% drift) displacement level, the strength degraded to less than 50% of the maximum capacity and the test was terminated.

### 3.2.5. Wall W5

This wall failed in a flexural ductile manner, but unfortunately, the strength when the wall was pushed to the west was degraded as seen in Fig. 3(d), as there were significant cracks in the foundations located in the East corner occurred at $2.6\Delta_y$ displacement level inducing a bar bond slip. Bracing was performed and the wall was successfully tested. However, the damage caused is explained later.

There was a minor error to determine the real yield displacement $\Delta_y$ due to the bond slip. The actual experimental yield displacement was later identified from the analysis of the experimental results and was used to quantify the corresponding actual displacement levels experienced by the wall. The wall experimental yield loads were 220 kN in the push and 270 kN in the pull, corresponding to lateral top displacements equal to 7.3 mm (0.18% top drift) and 9.2 mm (0.23% top drift) for the push and pull directions, respectively. At $2.6\Delta_y$ (0.84% drift) displacement level, the maximum capacity of the wall reached and equaled to 332 kN and 313 kN in the push and pull directions, respectively. At $3.7\Delta_y$ (0.85% drift) displacement level, the West corner flanged toe crushed and the bars buckled. During the loading to $5.1\Delta_y$ (1.15% drift) displacement level, 4 bars fractured in the flanged region located in the West toe as indicated in Table 4. The wall reached its ultimate level displacement at 52 mm (1.30% drift), while at $6.4\Delta_y$ (1.45% drift) displacement level, all the bars in the flanged area fractured in addition to 4 bars in the webs as shown in Fig. 4(e). At $8.0\Delta_y$ (1.80% drift) displacement level, the strength degraded to less than 50% of the maximum capacity and the test was terminated.

### 3.2.6. Wall W6

The wall yielded at 227 kN and 209 kN in the push and pull directions, respectively. The average $\Delta_y$ was taken equal to 10.5 mm (0.26% top drift). The hysteresis loops continued to widen and energy dissipation increased after yielding as shown in Fig. 3(f). The maximum load $Q_u$ was recorded at $3\Delta_y$ (0.79% drift) displacement level, and was equal to 334 kN in the push direction and 313 kN in the pull direction. At $4\Delta_y$ (1.05% drift) displacement level, uplift of the tension side was observed and minor concrete spalling was visible in the compression zone. At $5\Delta_y$ (1.32% drift) displacement level, toe crushing occurred at both ends of the wall

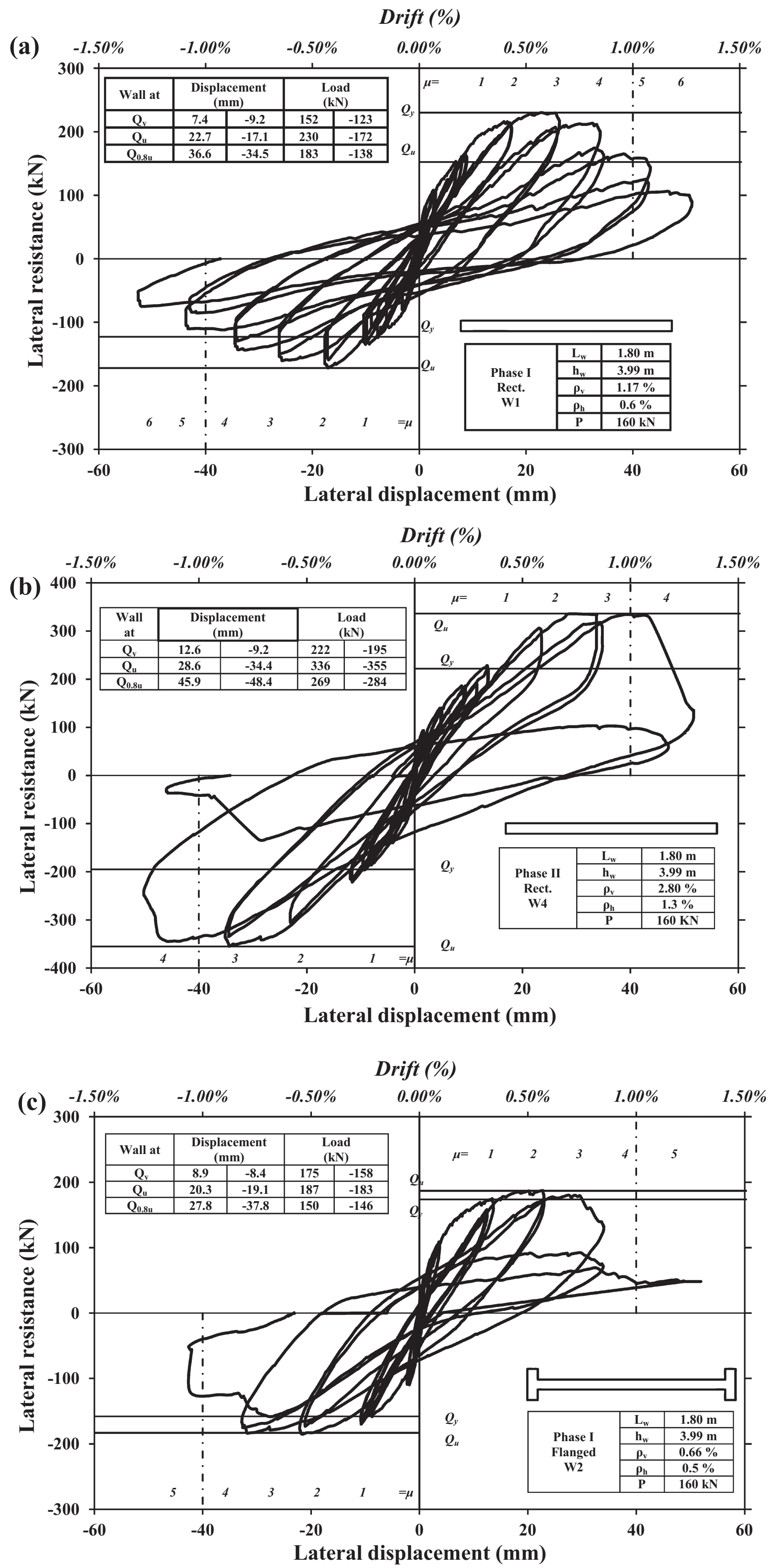


**Fig. 3.** Load–displacement relationships; rectangular walls (a) *W1* & (b) *W4*; flanged walls (c) *W2* & (d) *W5*; boundary elements walls (e) *W3* & (f) *W6*.

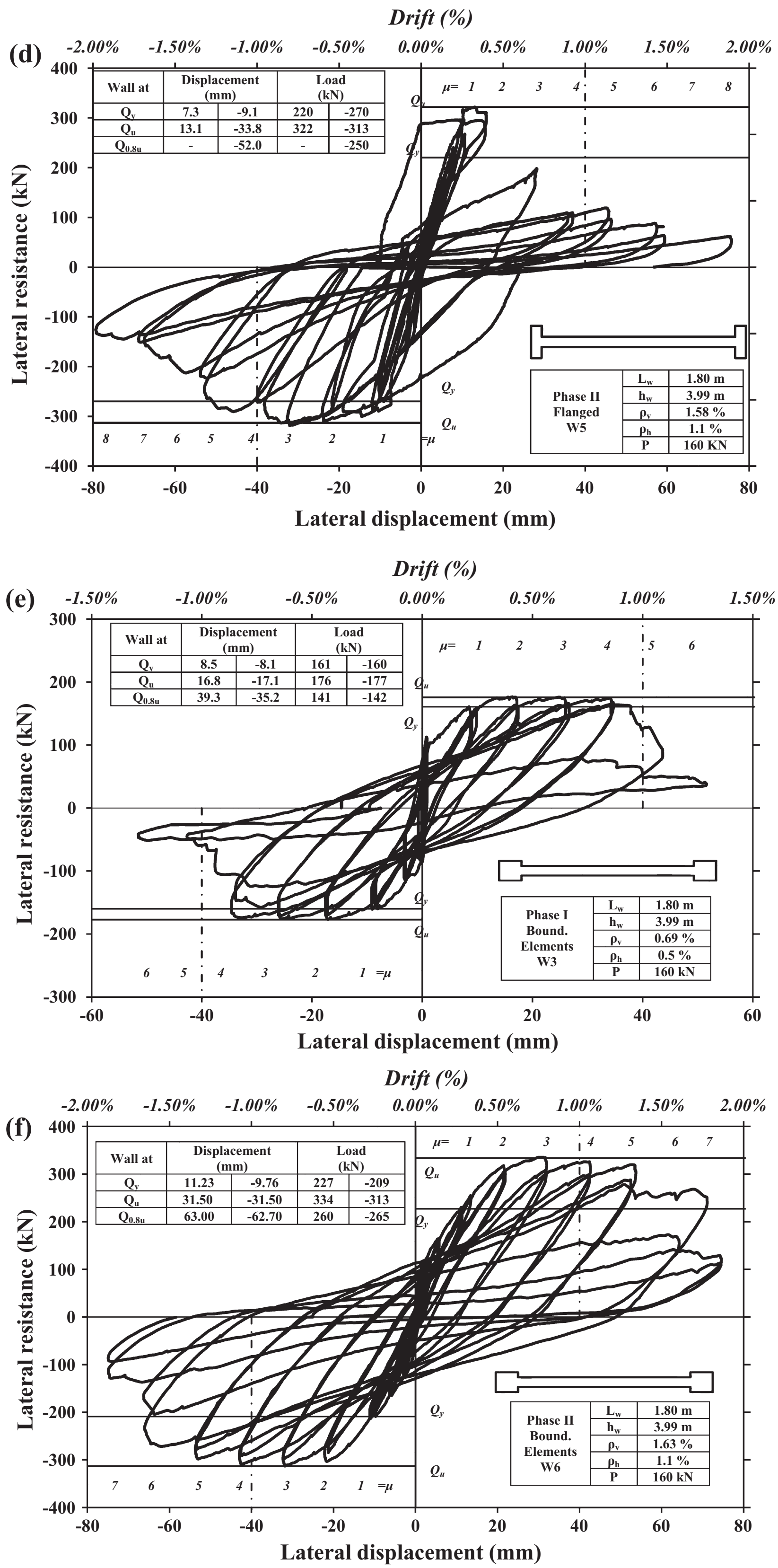


**Fig. 3** (*continued*)

and 7 reinforcement bars buckled in the East boundary element while 4 bars buckled in the West boundary element as shown in Fig. 4(f). At $6\Delta_y$ (1.58% drift) displacement level, 4 vertical reinforcement bars fractured in the East end and 2 others in the West end and the ultimate level displacement $\Delta_{0.8u}$ was reached as listed in Table 4. At, $8\Delta_y$ (2.1% drift) displacement level, all the vertical reinforcement bars in the confined regions fractured in addition to the outer four vertical bars in the East side and two

**Table 4**
Summary of experimental damage levels and the occurrence of the damage states after the stated loading cycle.

| Walls | Configuration | Experimental damage levels determined at the stated displacement level cycle* and % drift | | | | | | Damage states according to the Applied Technological Council (ATC P58, 2012) determined after the stated displacement level cycle | | | |
|---|---|---|---|---|---|---|---|---|---|---|---|
| | | Concrete spalling | | Concrete crushing | | Reinforcement fracture started | | *DS1* | *DS2* | *DS3* | *DS4* |
| | | Loading cycle | *Drift* (%) | Loading cycle | *Drift* (%) | Loading cycle | *Drift* (%) | | | | |
| *Phase I* | | | | | | | | | | | |
| *W1* | Rectangular | $3\Delta_y$ | 0.57 | $4\Delta_y$ | 0.84 | $4\Delta_y$ (*2nd Cycle*) | 0.84 | $2\Delta_y$ | $4\Delta_y$ | $5\Delta_y$ | $6\Delta_y$ |
| *W2* | Flanged | $3.5\Delta_y$ | 0.75 | $4.6\Delta_y$ | 1.00 | $4.6\Delta_y$ | 1.00 | $2.3\Delta_y$ | $3.5\Delta_y$ | $4.6\Delta_y$ | $5.8\Delta_y$ |
| *W3* | Boundary elements | $3\Delta_y$ | 0.63 | $4\Delta_y$ | 0.84 | $4\Delta_y$ (*2nd Cycle*) | 0.84 | $3\Delta_y$ | $4\Delta_y$ | $5\Delta_y$ | $6\Delta_y$ |
| *Phase II* | | | | | | | | | | | |
| *W4* | Rectangular | $3\Delta_y$ (*2nd Cycle*) | 0.84 | $4\Delta_y$ | 1.13 | $4\Delta_y$ (*2nd Cycle*) | 1.13 | $3\Delta_y$ | $4\Delta_y$ | | $4\Delta_y$ (*2nd Cycle*) |
| *W5* | Flanged | $2.6\Delta_y$ | 0.84 | $3.7\Delta_y$ | 0.85 | $5.1\Delta_y$ | 1.30 | $2.6\Delta_y$ | $3.7\Delta_y$ | $6.4\Delta_y$ | $8\Delta_y$ |
| *W6* | Boundary elements | $4\Delta_y$ | 1.05 | $5\Delta_y$ | 1.32 | $6\Delta_y$ | 1.58 | $3\Delta_y$ | $4\Delta_y$ | $6\Delta_y$ | $7\Delta_y$ |

* Damage occurred at the first displacement level cycle unless noted.

in the West sides of the wall web. Furthermore, the wall strength degraded to 50% of the maximum capacity and the test was terminated.

In *Phase II*, flanged wall ($\rho_v$ = 1.58%) and the wall with boundary elements ($\rho_v$ = 1.63%) developed hysteretic curves that showed higher energy dissipation when compared to their rectangular counterpart and when compared to *Phase I* flanged and boundary elements walls. Due to localized failure at the interface *Phase I* flanged ($\rho_v$ = 0.66%) and boundary elements ($\rho_v$ = 0.69%) walls did not show high-energy dissipation. Regarding the rectangular walls, *Phase I* Wall *W1* ($\rho_v$ = 1.17%) the hysteretic loops showed higher energy dissipation than wall *W4* ($\rho_v$ = 2.80%). The walls with boundary elements and flanges did not only experience an increased energy dissipation capacities, but also, due to their lesser/controlled damage in their respective compression zones, showed lesser pinching, than their rectangular wall counterparts.

Pinching in all the walls was minimal up to their respective maximum capacities. Beyond the drift corresponding to their maximum capacities, *Phase I* flanged and boundary elements walls showed higher pinching levels when compared to their *Phase II* counterparts due to the concentration of the primary crack located at the wall/base interface. This can be observed in the load–displacement relationships of the walls presented in Fig. 3(c) –(f). Minimal pinching occurred for all the walls after the crushing of the concrete at the toes. Regarding the rectangular walls, minimal pinching occurred at $4\Delta_y$ displacement level for both walls. While *Phase II* flanged Wall *W5*, Pinching was visible in Fig. 3(d) during the loading to $5.1\Delta_y$ (1.15% drift) displacement level. The hysteretic curves of the boundary element Wall *W6*, showed minimal pinching at $5\Delta_y$ (1.32% drift) displacement level. Regarding *Phase I* flanged and boundary elements walls pinching occurred at $4.6\Delta_y$ (1.00% drift) and $4\Delta_y$ (0.84% drift) displacement levels, respectively. With increasing pinching the observed damage of the walls increased and the confined region reinforcement bars buckled for all walls. Moreover, it increased relatively at higher displacement levels after the bars buckled up to the walls failure. Overall, pinching was minimized due to the high contribution of flexure when compared to shear in the formation of the hysteretic curves as agreed with Kolozvari et al. [21].

The flanged and the boundary elements walls in *Phase I* did not show the expected ductility when compared to its rectangular counterpart. That was due to the difference in failure when compared to *Phase II* walls as a primary flexural crack was observed at the interface located at the tensile portion of the wall. High tensile strain demand was required in the tensile portion of the wall, thus the primary crack at the interface occurred. As the wall toe region experience compression, the compression is resisted mainly by the boundary element and the flange of Walls *W3* and *W2* Walls, respectively, as a result of their webs instability. In other words, for these walls, the neutral axis remained within the boundary element or the flange, resisting higher compressive stresses, and thus strains, to maintain equilibrium. At higher ductility levels, the compressive toe experiences higher level of stresses, which resulted in concrete spalling of the boundary element and then only the inner confined area resists compression. After that, reinforcement bars typically buckled and the strength degraded rapidly. Subsequently, the walls failed without reaching their expected high inelastic displacement levels. In addition, as the walls developed primary flexural cracks, the plastic straining of the reinforcement was typically localized at the vicinity of crack. At higher displacement levels, the reinforcements experienced increased concentrated plastic deformation until fracture, which also limited the plastic hinge length, resulting in the unexpected low performance. This is consistent with the results of Gilbert and Smith [35], concluding that although the member is ductile in the critical cross-section, a non-ductile response due to the localization of the plastic deformation of the reinforcement bar was observed.

### 3.3. Cracks pattern

The first crack was observed at around 60% and 80% of the theoretical yield load of each wall. Up to the yield load most of the cracks were flexural cracks for *Phase I* walls, and at further loading, inclined shear cracks started to form. For *Phase I* walls, few flexural cracks were observed at the bottom half of the second story and minimal hairline diagonal shear cracks were observed within the second and third story. *Phase II* walls shown in Fig. 4(d)–(f) had extensive flexural and diagonal shear cracks compared to the *Phase I* walls shown in Fig. 4(a)–(c). For *Phase II* walls, Flexural cracks were visible over the entire first story and over the bottom half of the second story at 80%$F_y$ and diagonal shear cracks were observed over the first and the second story prior yielding. After first yield, more inclined shear cracks were observed over the first story, relatively less at the second story, and very few over the third story. For all the specimens once the concrete toe crushed few new cracks formed and existing cracks started to extend both in width and length. At such loading stage, the hysteresis loops would typically get wider as a result of the high energy dissipation due to crushing at the toes and buckling in the outermost vertical bars in addition to the widening of the existing cracks.

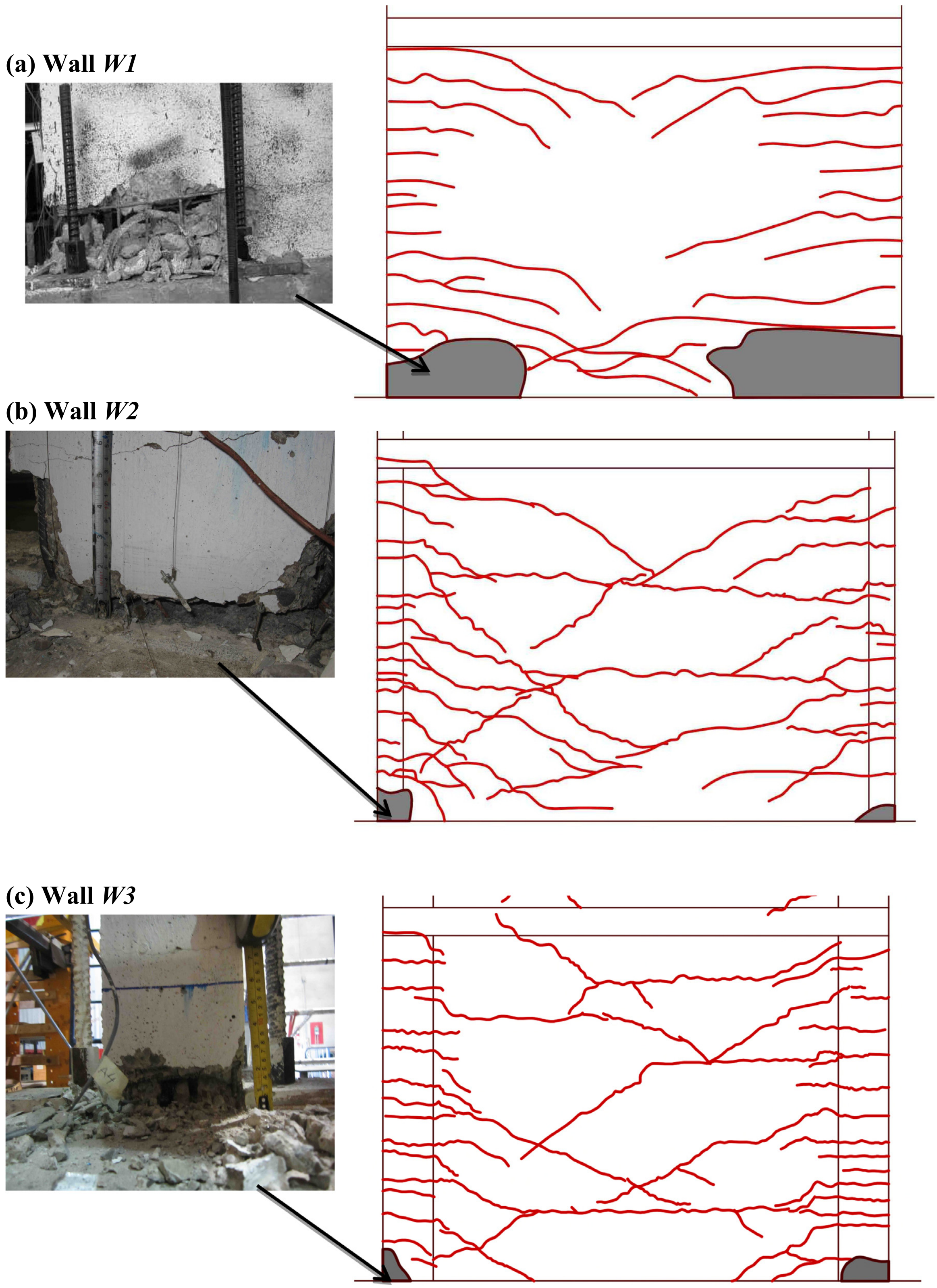


**Fig. 4.** First story crack patterns and toe damage at failure for each wall; (a) *W1*; (b) *W2*; (c) *W3*; (d) *W4*; (e) *W5*; (f) *W6*.



## 4. Analysis of experimental results

### 4.1. Walls damage quantification

According to the Federal Emergency Management Agency (*FEMA P*58) [36], damage states are related to the residual story drift and classified into four levels. The first damage state (*DS*1), is reached when non-structural repairs are needed and occurs when the story residual drift reach 0.2% the height of the story, whereas, the second damage state (*DS*2), is specified corresponds to story drift equal to 0.5% and when structural realignment and repairs are needed to limit degradation of the structure stability.

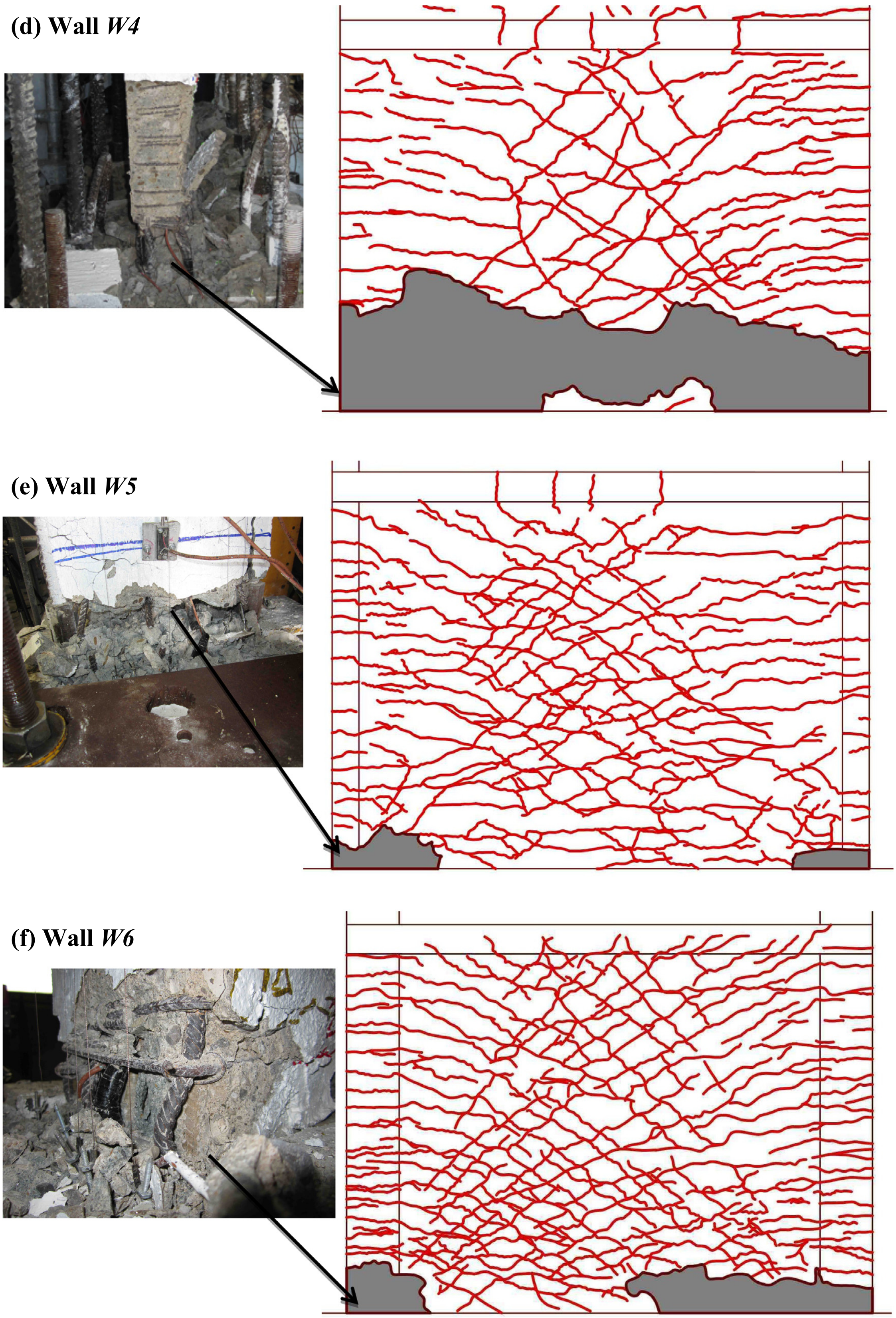


**Fig. 4** (*continued*)

The third damage state (*DS*3), is defined when a major structural realignment is required to restore the safety margin for lateral stability. At such a point the structure might be a total economic loss and expected to occur at 1% story drift. At *DS*3 the cost of repairs for the existing building exceeds the construction of a new one so it is more economical to build a new building. Finally, the fourth damage state (*DS*4), is reached when the residual drift is larger than 1% to the extent that the structure is in danger of collapse from seismic aftershocks. *DS*4, indicates that the building is on the verge of collapsing and structural repairs are not an option, therefore a new building is inevitable.

Table 4 shows the occurrence of each damage state while specimen was tested. The displacement level cycles written on the right side of Table 3 indicates that the selected specimen reached the specified damage state at the mentioned displacement cycle.

The first (*DS*1) and second (*DS*2) damage states, occurred at the same displacement ductility levels for all walls except for the rectangular walls where *DS*1 was reached at $2\Delta_y$ for Wall *W1* and $3\Delta_y$ for Wall *W4*. As seen in Table 4, *DS*3 for Wall *W4* was not reached as the wall reached its *DS*2 after the first $4\Delta_y$ displacement level cycle, however due to bar snapping, the wall was on the verge of collapsing *DS*4 after performing the second $4\Delta_y$ cycle. *Phase II* flanged and boundary elements walls showed higher displacement ductility levels for higher damage states when compared to their *Phase I* counterparts. This reflects the enhanced seismic performance of both the flanged Wall *W5* with higher reinforcement ratio ($\rho_v\% = 1.58$) and the boundary elements Wall *W6* ($\rho_v\% = 1.63$). On the other hand, for the rectangular walls, higher ductility levels corresponding to the *DS*3 and *DS4* levels were achieved by Wall *W1* ($\rho_v\% = 1.17$) when compared to those of Wall *W4* ($\rho_v\% = 2.80$). Moreover, relatively higher reinforcement ratio and well-distributed web reinforcement of flanged and boundary elements walls would reach the damage state levels at higher ductility levels.

### 4.2. Load–displacement envelopes

Load displacement relationships for each specimen were constructed and compared in Fig. 5. The cross sectional configuration of the flanged and the boundary elements Walls (*W2* and *W3*) having less vertical reinforcement ratio compared to rectangular Wall *W1*, were expected to show higher ductile capability but due to the localized cracking between the wall and the foundation, which concentrated the steel plastic strain at the interface, these walls did not show the intended seismic performance. As shown in Fig. 5(b), the rectangular Wall *W4* had a lower ductile capability and lower ultimate drift when compared to the flanged Wall *W5* and the wall with boundary elements *W6*. The increase in the drift ratios of Walls *W5* and *W6* was due to the configuration and the confinement of the horizontal hoops at the heavily reinforced regions. It can be inferred that flanges and boundary elements enhance the structural wall performance allowing the wall to reach higher drifts with slower strength degradation rate. As shown in Figs. 5(b) and 6(b), *W5* load displacement envelope in the push direction was not added in the comparison due to foundation cracks as mentioned earlier in *W5* load–displacement relationships section.

To facilitate comparison between the walls, the load was normalized for each specimen, as *Phase II* wall strengths were higher than those in *Phase I*. As shown in Fig. 6 *Phase II* walls had higher displacement (top drifts) compared to *Phase I* walls at both maximum and ultimate load capacities. The reasons of such higher displacements were related to the effect of the primary cracks leading to concentration of the steel plasticity at those locations and consequently localizing the plastic curvature and the plastic hinge length over a relatively small height above the foundation level. While for *Phase II* higher vertical reinforcement forced the walls to initiate larger number of horizontal flexural cracks as well as diagonal shear cracks in addition to secondary flexural cracks. These secondary cracks distributed the high tensile in the outermost vertical reinforcement over a larger length, which resulted in spreading the high curvatures at the base of the wall over a larger zone and extended the plastic hinge length. Such a phenomenon resulted in turn in increased top displacements

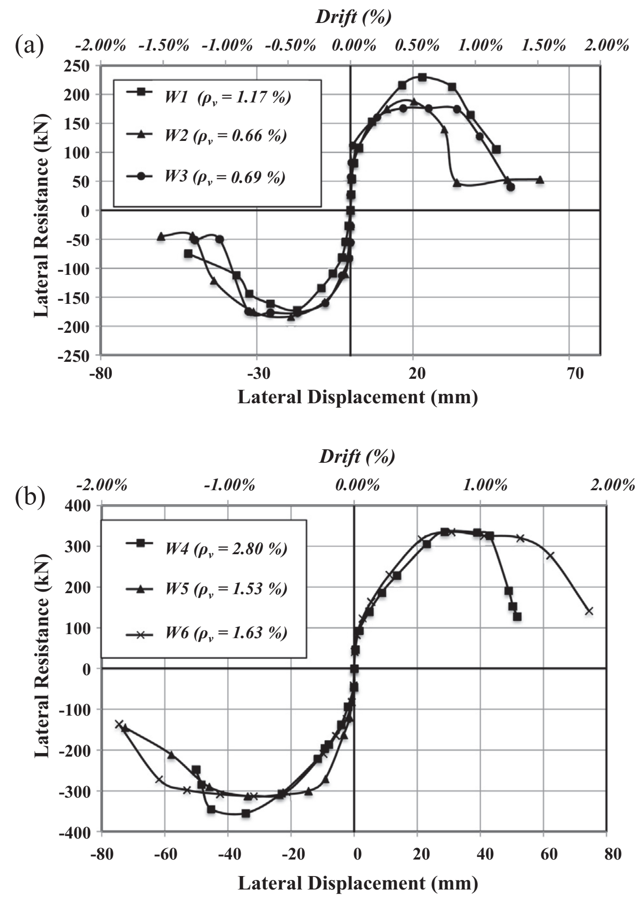


**Fig. 5.** Load–displacement envelopes; (a) *Phase I*; (b) *Phase II*.

corresponding to maximum and ultimate capacities for walls with higher reinforcement ratios as opposed to those with lower ratios. The discussed results agree with the Canterbury Report [1].

Table 5 showed the yield displacement $\Delta_y$, displacement at the maximum load $\Delta_u$ and ultimate displacement at 20% strength degradation $\Delta_{0.8u}$ as well as the corresponding percentage drifts. The yield displacement for all the walls varied between 8.3 mm and 10.9 mm (0.21–0.27% drift). The maximum loads were reached for *Phase I* walls at top drifts varying between 0.42% and 0.69%, while, *Phase II* wall maximum loads achieved at top drifts varying between 0.72% and 0.86%. Drifts corresponding to ultimate displacement (at 20% strength degradation) for *Phase I* varied between 0.70% and 0.98% while varied between 1.15% and 1.58% for *Phase II* specimens. As discussed it was clear that *Phase II* had higher top displacements at maximum load and at 20% strength degradation when compared to *Phase I* walls.

### 4.3. Displacement ductility

The seismic performance could better be quantified by evaluating the displacement ductility values, as high ultimate displacement values do not necessarily imply high ductility capacities. The experimental displacement ductility values in this section were computed by dividing the displacement at the target displacement level ($\Delta$) by the yield displacement ($\Delta_y$). The yield displacement ($\Delta_y$) was the lateral displacement when the first outermost vertical reinforcement started yielding. The displacement ductility values for all the walls at the maximum load $\mu_\Delta$ and at 20% strength degradation (ultimate displacement) $\mu_{\Delta 0.8u}$ are presented in Fig. 7. The displacement ductility covers fully the kinetic energy dissipated from the structural wall.

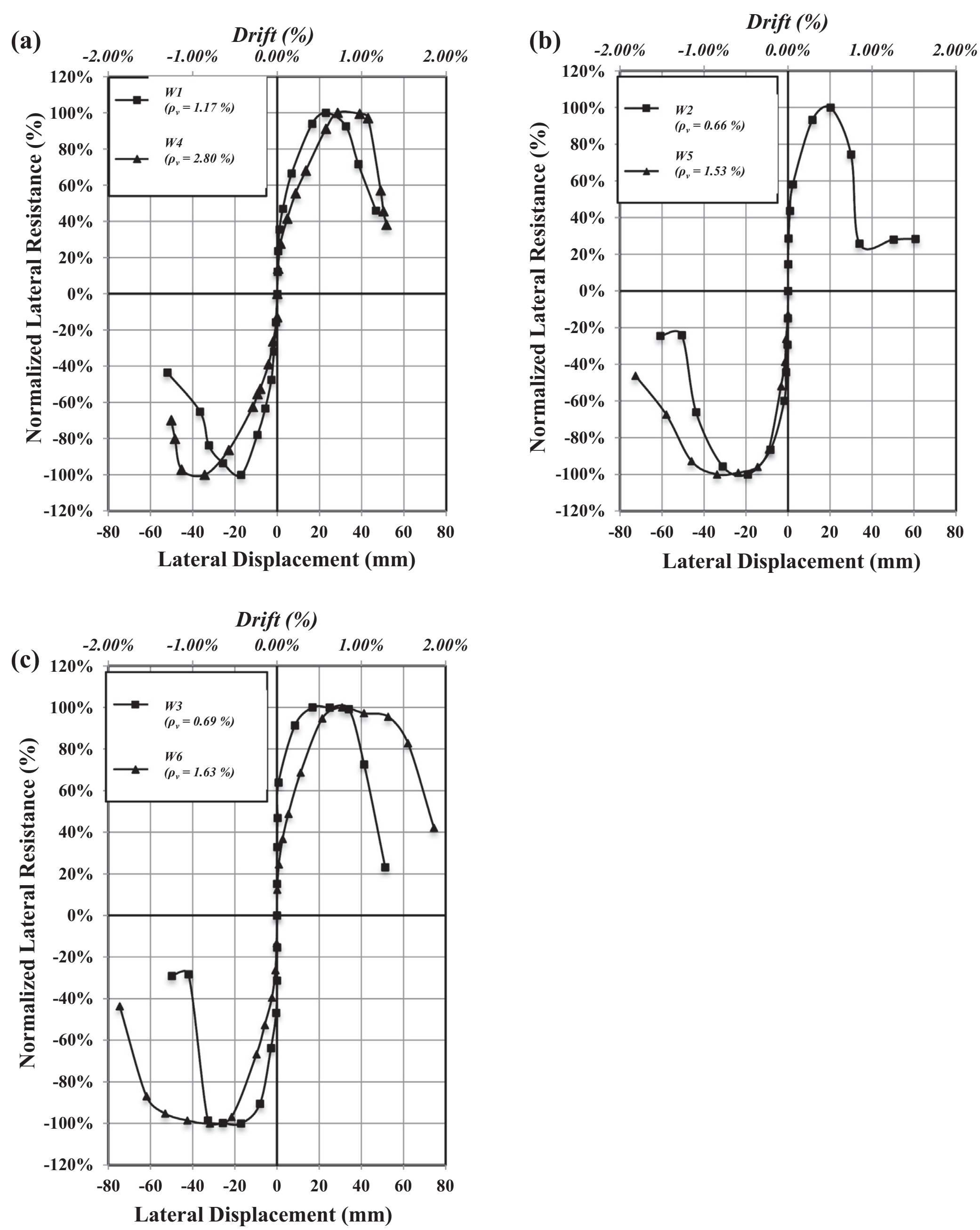


**Fig. 6.** Normalized load–displacement relationships; (a) rectangular walls *W1* & *W4*; (b) flanged walls *W2* & *W5*; (c) boundary elements walls *W3* & *W6*.

The displacement ductility values calculated at the maximum load $\mu_\Delta$ varied between 2.0 and 2.7 in *Phase I* walls, and between 2.6 and 3.7 for walls in *Phase II* as indicated in Table 5. The displacement ductility values at ultimate displacements $\mu_{\Delta 0.8u}$ for *Phase I* walls ranged between 3.2 and 4.7 whereas for *Phase II* walls, $\mu_{\Delta 0.8u}$ varied between 4.2 and 6.0. As such, it is clear in *Phase II* that the displacement ductility values attained by the flanged and boundary elements walls were, respectively 33% and 40% higher than that attained by their rectangular counterpart. The reason for the higher ductile capacity was the confinement and the configuration of the flanges and the boundary elements, which confined the concrete from crushing at earlier stages and enabled sustaining the lateral load capacity at high drift levels. On the other hand, the similar ductility values for *Phase I* could be justified based on the generation of the primary cracks at the interface for walls *W2* and *W3* that controlled the failure and limited the ductility due to high plastic strains concentrated in a relatively smaller length and the relatively low number of bars, acting as dowels between the foundation and the base of the wall, controlling the sliding after generation of the primary crack extending over the entire length of these walls.

### 4.4. Idealized displacement ductility

The idealized displacement ductility values $\mu_\Delta^{id}$ were determined based on bilinear idealization (elastic-perfectly plastic system) performed by Priestley et al. [33]. It offers a conservative yield displacement value, which is the intersection of the yield stiffness $K_y$ line of slope with a horizontal line from the maximum capacity $Q_u$. The maximum capacity idealized displacement ductility $\mu_{\Delta u}^{id}$ was determined by dividing the lateral displacement at the

**Table 5**
Yield displacement, ultimate displacement, displacement ductility and idealized displacement ductility.

| Wall | Configuration | Direction | At first yield | | At maximum load | | | | At 20% strength degradation | | | |
|---|---|---|---|---|---|---|---|---|---|---|---|---|
| | | | $\Delta_y$ (mm) | % Drift | $\Delta_u$ (mm) | $\mu_\Delta$ | % Drift | $\mu^{id}_{\Delta u}$ | $\Delta_{0.8u}$ (mm) | $\mu_{\Delta 0.8u}$ | % Drift | $\mu^{id}_{\Delta 0.8u}$ |
| *Phase I* | | | | | | | | | | | | |
| *W1* | Rectangular | +(ve) | 8.3 | 0.21 | 22.7 | 2.7 | 0.57 | 1.8 | 36.6 | 4.4 | 0.92 | 2.9 |
| | | −(ve) | | | 17.1 | 2.1 | 0.43 | 1.5 | 34.5 | 4.2 | 0.86 | 3.0 |
| *W2* | Flanged | +(ve) | 8.7 | 0.22 | 20.3 | 2.4 | 0.51 | 2.2 | 27.8 | 3.2 | 0.70 | 3.0 |
| | | −(ve) | | | 19.1 | 2.2 | 0.48 | 1.9 | 37.8 | 4.4 | 0.95 | 3.8 |
| *W3* | Boundary elements | +(ve) | 8.3 | 0.21 | 16.8 | 2.0 | 0.42 | 1.8 | 39.3 | 4.7 | 0.98 | 4.3 |
| | | −(ve) | | | 17.1 | 2.1 | 0.43 | 1.9 | 35.2 | 4.2 | 0.88 | 3.8 |
| *Phase II* | | | | | | | | | | | | |
| *W4* | Rectangular | +(ve) | 10.9 | 0.27 | 28.6 | 2.6 | 0.72 | 1.7 | 45.9 | 4.2 | 1.15 | 2.8 |
| | | −(ve) | | | 34.4 | 3.2 | 0.86 | 1.8 | 48.4 | 4.4 | 1.21 | 2.4 |
| *W5* | Flanged | +(ve) | 9.1 | 0.23 | – | – | – | – | – | – | – | – |
| | | −(ve) | | | 33.8 | 3.7 | 0.85 | 3.2 | 52 | 5.7 | 1.30 | 4.9 |
| *W6* | Boundary elements | +(ve) | 10.5 | 0.26 | 31.5 | 3.0 | 0.79 | 2.0 | 63.0 | 6.0 | 1.58 | 4.1 |
| | | −(ve) | | | 31.5 | 3.0 | 0.79 | 2.0 | 62.7 | 6.0 | 1.57 | 4.0 |

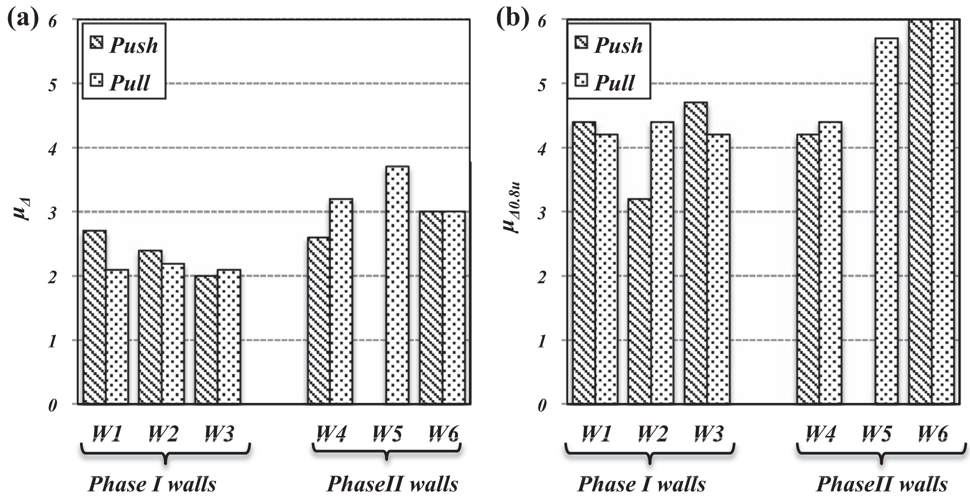


**Fig. 7.** Walls displacement ductility values: (a) At maximum capacity; (b) At ultimate level.

maximum by the idealized yield displacement. While the ultimate level idealized displacement ductility $\mu^{id}_{\Delta 0.8u}$ was the lateral displacement at 20% strength degradation by the idealized yield displacement.

The idealized displacement ductility at the maximum capacity $\mu^{id}_{\Delta u}$ varied between 1.5–2.2 and 1.7–3.2 for *Phase I* and *Phase II*, respectively as listed in Table 5. *Phase I* flanged Wall *W2* achieved higher $\mu^{id}_{\Delta u}$ by 24% when compared to rectangular Wall *W1*. While the boundary elements Wall *W3* showed similar $\mu^{id}_{\Delta u}$ in the push direction and showed 1.26 times the rectangular $\mu^{id}_{\Delta u}$ value in the pull direction. In *Phase II*, the flanged and the walls with boundary elements average higher than their rectangular counterpart by 1.8 and 1.2 times, respectively. Regarding the idealized displacement ductility value at 20% strength degradation $\mu^{id}_{\Delta 0.8u}$, *Phase I* walls varied between 2.9 and 4.3 while *Phase II* walls ranged from 2.4 to 4.9 as listed in Table 5. *Phase I* boundary element Wall *W3* average $\mu^{id}_{\Delta 0.8u}$ was 1.4 times the rectangular Wall *W1* idealized displacement ductility. While the flanged wall resulted in 1.3 times, the rectangular value in one direction and the same $\mu^{id}_{\Delta 0.8u}$ value in the other. *Phase II* flanged and boundary elements walls achieved higher average $\mu^{id}_{\Delta 0.8u}$ when compared to their rectangular counterpart by 90% and 60%, respectively.

*Phase II* showed higher average idealized displacement values at maximum capacity and compared to *Phase I* walls. While the average idealized displacement ultimate level $\mu^{id}_{\Delta 0.8u}$ of *Phase II* were, higher than *Phase I* walls for the flanged walls by 44%, similar to the boundary elements walls and slightly lower by 10% than the rectangular walls.

Flanged and boundary elements walls in *Phase II* showed an enhanced seismic performance when compared to their rectangular counterpart. That was due to the well-detailed flange and boundary element for Walls *W5* and *W6* respectively. Larger confined area was able to resist the increasing compressive stress delaying buckling of the confined region due to adequate transverse reinforcement and hoops detailing. Moreover, due to the higher concentration of reinforcement at the confined region of the boundary elements and within the flange of the flanged walls, the walls were more capable of meeting higher tensile strain demands when compared to the rectangular Wall *W4*. Hence, *Phase II* flanged and boundary elements walls experienced an enhanced seismic performance. Furthermore, it is essential to reinforce the web region adequately to expect higher seismic performance, as Walls *W2* and *W3* did not show the expected ductility capacity when compared to their rectangular counterpart Wall *W1* due to a localized flexural primary crack, where the plastic straining of the reinforcements was localized at the primary crack locations.

### *4.5. Stiffness degradation*

Fig. 8 shows the stiffness degradation from yield to failure of each wall versus displacement levels $\Delta/\Delta_y$. At yield $K_y$, ranged

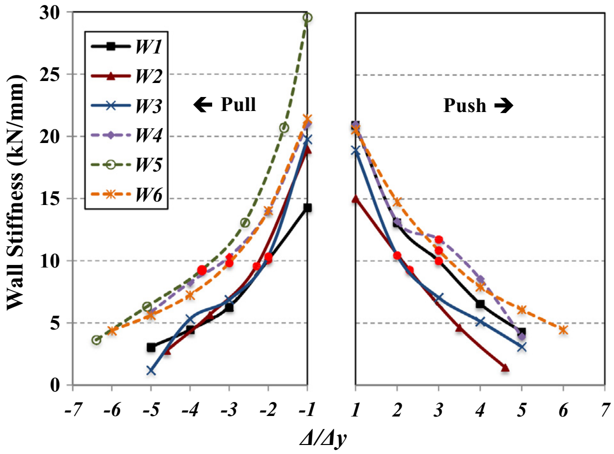


**Fig. 8.** Stiffness degradation versus displacement levels $\Delta/\Delta_y$.

between 14.3 and 30.1 kN/mm, while at the ultimate loads $K_u$ varied between 9.3 and 11.8 kN/mm for all the specimens shown as red points in Fig. 8. The stiffness at 20% strength degradation $K_{0.8u}$ for all the walls was between 2.0 and 7.6 kN/mm. It was observed that both rectangular walls had higher $K_{0.8u}$ when compared to the flanged and the boundary elements walls for both Phases. This implies that the flanged and boundary elements walls would attract less base shear at higher displacement levels when compared to the rectangular walls. Fig. 8 shows that *Phase II* walls have higher stiffness values at the ultimate level $K_{0.8u}$ when compared to their *Phase I* counterparts. All the specimens resulted in similar stiffness values at the maximum load $K_u$. As shown in Fig. 8, the stiffness degrades on higher rate for *Phase I* walls when compared to their *Phase II* counterparts, which is due to the difference in the intensity of failure between *Phase I* and *Phase II* walls. *Phase II* walls had extensive cracks and crushing of the concrete, which lowered the stiffness degradation rate when compared to *Phase I* walls in which walls primary cracks at the interface accelerated the stiffness degradation. When comparing the stiffness degradation for the walls on each phase, similar stiffness degrading slopes were observed, as shown in Fig. 8, which illustrates that the design base shear should be similar for all the walls at each phase. Due to foundation cracks mentioned earlier for flanged wall *W5*, the stiffness degradation values in the push direction were not considered.

## 5. Conclusions

Strength prediction for the walls using the Canadian code *CSA A23.3-14* [3] showed an excellent agreement with the experimental strengths. At the primary crack location between the base and the wall, the strain in the steel kept increasing till the steel fractured and the concrete crushed over a small height.

The ductile capability for *Phase II* walls were better than *Phase I* walls when comparing the normalized load–displacement envelopes which is consistent with the Canterbury earthquake observations for walls with higher reinforcement ratios.

The displacement ductility values at 20% strength degradation $\mu_{\Delta 0.8u}$ of the rectangular, flanged wall and wall with boundary elements with low reinforcement ratios were almost similar, however for walls in *Phase II* with higher reinforcement ratios, the attained displacement ductility values by the flanged and boundary elements walls were 50% and 33% higher than their counterparts in *Phase I*.

The displacement ductility values of the flanged wall *W5* and boundary elements *W6* walls seismic performances were respectively 33% and 40% higher than their rectangular counterpart *W4*. While, the average idealized displacement ductility values of the flanged and boundary elements walls were higher than their rectangular counter parts by 40% and 30% for *Phase I* walls and 90% and 60% for *Phase II* walls, respectively. Such findings are in line with those reported in the Canterbury Earthquake Royal Commission report [1], which recommended concentrating the vertical reinforcements in the outer regions. Generally, Wall end-configurations have major effects on the seismic performance; boundary elements and flanged walls tend to have higher seismic performance. This is due to the larger confined area when compared to rectangular walls. In effect, larger confined areas are able to resist the increasing compressive forces when the cantilever wall is loaded in-plane to higher displacement levels. Moreover, due to higher concentration of the vertical reinforcement at the confined region, the walls could resist higher tensile strains so that the walls could achieve higher ductility capacities. The end-configurations tend to delay the strength degradation at higher displacement level, which, in turn, enhances the seismic performance of the walls.

By increasing the vertical reinforcement ratio in *Phase II* compared to what in *Phase I*, secondary cracks were observed and the steel strain was more uniformly distributed at higher length, which increased the ductile capability of the seismic force resisting structural walls. These results are also in agreement with the Canterbury Commission report recommendations [1] of the need to increase the vertical reinforcement ratio $\rho_v\%$ to initiate secondary cracks to extend the plastic hinge length and therefore better seismic performance can be achieved. It is essential to adequately reinforce the web region of the wall to prevent any bond slip of the webs and to extend the plastic straining on multiple flexural cracks instead of strain localization in the vicinity of the primary flexural crack. As such, the provisions for minimum web reinforcement of seismically-detailed *RC* walls might need to be revisited.

Future editions of seismic codes might need to consider assigning different values for the ductility-related modification factor $R_d$ for ductile walls with different configurations and related to different vertical reinforcement ratio. However, due to the limited number of specimens tested within the current study, further research is necessary to develop recommendations for code revision.

## Acknowledgments

Financial support has been provided by the McMaster Centre for Effective Design of Structures (CEDS) funded through the Ontario Research and Development Challenge Fund (ORDCF) as well as the Natural Sciences and Engineering Research Council (NSERC) of Canada.

## Appendix A. Theoretical yield load calculations

Compression in concrete

$$Cc = \text{Triangular Area} \times \varepsilon_c \times E_c = \left(\frac{1}{2} b \cdot c\right) \cdot \varepsilon_c \cdot E_c$$

Where, concrete compressive strain

$$\varepsilon_c = \frac{c(\varepsilon_y)}{(a_1 - c)}$$

And concrete Young's modulus

$$E_c = 4500\sqrt{f'_c}$$

Moment of concrete,

$$M_{yconc} = C_c\left(\frac{l_w}{2} - \frac{c}{3}\right)$$

Tensile force in the reinforcement at point $n$,

$$F_{sn} = A_{sn} \cdot \varepsilon_{sn} \cdot E_s$$

Sum of moments of the vertical reinforcements around the centroid ($M_{steel}$)

$$M_{steel} = \sum_{a_n \geqslant \frac{l_w}{2}}^{n=1,2,3,\ldots} (F_{sn})\left(a_n - \frac{l_w}{2}\right) + \sum_{a_n \geqslant \frac{l_w}{2}}^{n=1,2,3,\ldots} (F_{sn})\left(\frac{l_w}{2} - a_n\right)$$

So the theoretical yield strength

$$Q_{yth} = \frac{M_{steel} + M_{conc}}{h}$$

## Appendix B. Theoretical maximum capacity calculations

Compression in concrete

$$Cc = \alpha_1 f'_c \beta_1 cb$$

where

$$\alpha_1 = 0.85 - (0.0015f'_c) \quad [CSA\ A23.3\text{-}14]$$

$$\beta_1 = 0.97 - (0.0025f'_c) \quad [CSA\ A23.3\text{-}14]$$

Moment of concrete,

$$M_{conc} = C_c\left(\frac{l_w}{2} - \frac{\beta_1 c}{2}\right)$$

Tensile force in the reinforcement at a point $n$,

$$\{\text{for } \varepsilon_{sn} \geqslant \varepsilon_y, \text{ then use } \varepsilon_y\}$$

$$\{\text{for } -\varepsilon_y < \varepsilon_{sn} < \varepsilon_y, \text{ then use } \varepsilon_{sn}\}$$

$$\{\text{for } \varepsilon_{sn} \leqslant -\varepsilon_y, \text{ then use} -\varepsilon_y\}$$

$$F_{sn} = A_{sn} \cdot \varepsilon_{sn} \cdot E_s$$

Sum of moment of the reinforcements around the centroid $M_{steel}$

$$(M_{steel}) = \sum_{a_n \geqslant \frac{l_w}{2}} (F_{sn})\left(a_n - \frac{l_w}{2}\right) + \sum_{a_n < \frac{l_w}{2}} (F_{sn})\left(\frac{l_w}{2} - a_n\right)$$

So the theoretical maximum capacity ($Q_{uth}$)

$$Q_{uth} = \frac{M_{steel} + M_{conc}}{h}$$

$a_1$ = distance from the outermost tensile vertical reinforcements to the end of the compression toe (mm)
$a_n$ = distance from the vertical reinforcement at point $n$ to the end of the compression toe (mm)
$A_{sn}$ = vertical reinforcement cross-sectional area at point $n$ (mm$^2$)
$b$ = width of the section (mm)
$c$ = distance from the compression toe to the neutral axis (mm)
$C_c$ = compressive force due to concrete (mm)
$E_c$ = concrete modulus of elasticity (MPa)
$E_s$ = reinforcement steel modulus of elasticity (MPa)
$f'_c$ = concrete compressive strength (MPa)
$F_{sn}$ = tensile or compressive force of the reinforcements located at point $n$ (kN)
$h$ = height of the wall (mm)
$l_w$ = length of the wall (mm)
$M_{conc}$ = compressive concrete moment around the centroid (kN mm)
$M_{steel}$ = sum of moments of the vertical reinforcements around the centroid (kN mm)
$M_{yconc}$ = compressive concrete moment around the centroid at yield (kN mm)
$n$ = numbering of reinforcement locations, where $n$ = 1 is referring the outer most vertical reinforcement, $n$ = 2 refers to the second outermost vertical reinforcement, etc.
$Q_{yth}$ = theoretical yield strength (kN)
$Q_{uth}$ = theoretical maximum capacity (kN)
$\alpha_1$ = ratio of average stress in rectangular compression block to the specified concrete strength
$\beta_1$ = ratio of depth of rectangular compression block to depth to the neutral axis
$\varepsilon_c$ = concrete compressive strain
$\varepsilon_{sy}$ = reinforcement yield strain

## References

[1] Canterbury Earthquake Royal Commission report. Seismic performance Christchurch building under the Canterbury Earthquake. <http://canterbury.royalcommission.govt.nz/Final-Report-Volume-One-Contents> [retrieved 19.11.13].
[2] Standards New Zealand (NZS 3101). Concrete Structures Standard. Wellington, NZ; 2006.
[3] Canadian Standards Association (CSA). Design of concrete structures. CSA A23.3-14, Mississauga, ON, Canada; 2014.
[4] Jünemann R, Hube M, De La Llera JC, Kausel E. Characteristics of reinforced concrete shear wall buildings damaged during 2010 Chile earthquake. In: The fifteenth world conference on earthquake engineering, Lisbon, Portugal; 2012.
[5] Wallace JW, Massone LM, Bonelli P, Dragovich J, Lagos R, Lüders C, Moehle J. Damage and implications for seismic design of RC structural wall buildings. Earthquake Spectra J 2012;28(S1):S281–99.
[6] Carpenter LD, Naeim F, Lew M, Youssef NF, Rojas F, Saragoni GR, Adaros MS. Performance of tall buildings in Viña del Mar in the 27 February 2010 offshore Maule, Chile earthquake. Struct Des Tall Special Build J 2010;20:17–36.
[7] Thomsen JH, Wallace JW. Displacement-based design of RC structural walls: experimental studies of walls with rectangular and T-shaped cross sections. Report No. CU/CEE-95/06. Potsdam, N.Y.: Department of Civil and Environmental Engineering, Clarkson University; 1995. p. 353.
[8] Thomsen JH, Wallace JW. Displacement-Based Design of Slender Reinforced Concrete Structural Walls—Experimental Verification. J Struct Eng 2004;130(4):618–30.
[9] Massone L, Wallace J. Load-Deformation Responses of Slender Reinforced Concrete Walls. ACI Struct J 2004;101(4):512–20.
[10] Zhang Y, Zhihao W. Seismic Behavior of Reinforced Concrete Shear Walls Subjected to High Axial Loading. ACI Struct J 2000;97:739–50.
[11] Adebar P, Ibrahim A, Michael B. Test of High-Rise Core Wall: Effective Stiffness for Seismic Analysis. ACI Struct J 2007;104(5):549–59.
[12] Sittipunt C, Wood SL, Lukkunaprasit P, Pattararattanakul P. Influence of Web Reinforcement on the Cyclic Response of Structural Walls. ACI Struct J 2001;92:745–56.
[13] White TW. Seismic demand in high-rise concrete walls PhD Thesis. Department of Civil Engineering, University of British Columbia; 2004.
[14] Beyer K, Dazio A, Priestley MJN. Quasi-static cyclic tests of two u-shaped reinforced concrete walls. J Earthquake Eng 2008;12:1023–53.
[15] Preti M, Giuriani E. Ductility of a structural wall with spread rebars tested in full scale. J Earthquake Eng 2011;15:1238–59.
[16] Liao FY, Han LH, Zhong T. Performance of reinforced concrete shear walls with steel reinforced concrete boundary columns. Eng Struct 2012;44:186–209.
[17] Oh YH, Han SW, Lee LH. Effect of boundary element details on the seismic deformation capacity of structural walls. Earthquake Eng Struct Dyn 2002;31:1583–602.
[18] Orakcal K, Wallace JW, Conte JP. Flexural modeling of reinforced concrete walls-model attributes. ACI Struct J 2004. 101-688-98.
[19] Orakcal K, Wallace JW. Flexural modeling of reinforced concrete walls-experimental verification. ACI Struct J 2006;103(2):169–206.
[20] Kolozvari K, Kutay Orakcal K, Wallace JW. Modeling of cyclic shear-flexure interaction in reinforced concrete structural walls. I: Theory. ASCE J Struct Eng 2015;141(5):04014135.
[21] Kolozvari K, Kutay Orakcal K, Wallace JW. Modeling of cyclic shear-flexure interaction in reinforced concrete structural walls. II: Experimental validation. ASCE J Struct Eng 2015;141(5):04014136.
[22] Paulay T, Uzumeri SM. A critical review of the seismic design provisions for ductile shear walls of the Canadian code and commentary. Can J Civ Eng 1975;2:592–601.
[23] Paulay T. Seismic response of structural walls: recent developments. Can J Civ Eng 2001;28:922–37.

[24] Mitchell D, Tremblay R, Karacabeyli E, Paultre P, Saatcioglu M, Donald L, Anderson DL. Seismic force modification factors for the proposed 2005 edition of the National Building Code of Canada. Can J Civ Eng 2003;30(1):308–27.

[25] Mitchell D, Paultre P, Tinawi R, Saatcioglu M, Tremblay R, Kenneth Elwood, Adams J, DeVall R. Evolution of seismic design provisions in the National building code of Canada. Can J Civ Eng 2010;37(1):1157–70.

[26] Adebar P, Mutrie J, DeVall R. Ductility of concrete walls: the Canadian seismic design provisions 1984 to 2004. Can J Civ Eng 2005;32(2):1124–37.

[27] Ghorbanirenani I, Tremblay R, Léger P, Leclerc M. Shake table testing of slender RC shear walls subjected to Eastern North America seismic ground motions". ASCE J Struct Eng 2012;138(12):1515–29.

[28] Lu H, Leger P, Tremblay R. Seismic demand of moderately ductile reinforced concrete shear walls subjected to high frequency ground motions. Can Civil Eng 2014;41(2):125–35.

[29] NBCC: National Research Council of Canada, National Building Code of Canada; 2010.

[30] Paulay T, Priestley M. Seismic design of reinforced concrete and masonry buildings. New York: Wiley; 1992.

[31] American Society for Testing and Materials (ASTM). Standard test method for compressive strength of cylindrical concrete specimens. C39/C39M-10. West Conshohocken, PA: ASTM International; 2010.

[32] American Society for Testing and Materials (ASTM). Standard specification for deformed and plain carbon-steel bars for concrete reinforcement. A615/A615M-09b. West Conshohocken, PA: ASTM International; 2009.

[33] Priestley MJN, Calvi GM, Kowalsky MJ. Displacement based seismic design of structures. Pavia, Italy: IUSS Press; 2007.

[34] Shedid M, El-Dakhakhni WW. Plastic hinge model and displacement-based seismic design parameter quantifications for reinforced concrete block structural walls. ASCE J Struct Eng 2014;140(4):04013090.

[35] Gilbert RI, Smith ST. Strain localization and its impact on the ductility of reinforced concrete slabs containing welded wire reinforcement. Adv Struct Eng J 2006;9(1):117–27.

[36] Federal Emergency Management Agency (FEMA P58). Seismic performance assessment of buildings: damage states for residual story drifts. Washington D.C., USA: Federal Emergency Management Agency (FEMA) 356; 2012.